coatings

Article

Effect of Oblique LSP on the Wear Resistance of Plasma-Nitrided H13 Tool Steel

Longhui Li, Dongyan Lin *, Judong Liu, Junying Chen, Zhilong Xu, Shiqi Chen, Qingshan Jiang, Xiuyu Chen, Wenjun Jiang and Wenbin Ma

College of Marine Equipment and Mechanical Engineering, Jimei University, Xiamen 361000, China
* Correspondence: ldyscut@163.com

Abstract

H13 tool steel is widely used in precision injection molds; however, severe wear in confined regions, such as ejector pin holes, limits its service life, while conventional strengthening techniques remain difficult to apply in these areas. In this study, a combined plasma nitriding and oblique laser shock peening (OLSP) treatment was proposed, and the effects of laser incidence angle on microstructure, mechanical properties, and wear behavior were systematically investigated through electron backscatter diffraction (EBSD), X-ray diffraction (XRD) residual stress analysis, and ball-on-disk (BOD) wear tests. The results demonstrate that OLSP promotes grain refinement, dislocation accumulation, and the introduction of high-magnitude compressive residual stress. The NLSP1 sample exhibited the optimum strengthening effect, with a maximum compressive residual stress of −1033 MPa. It also achieved the lowest wear depth, wear volume, and specific wear rate, with a specific wear rate of 1.64×10^{-6} $mm^3/(N \cdot m)$, representing a 54.3% reduction compared with the untreated sample. The enhanced wear resistance was attributed to the synergistic effects of hardness improvement, microstructural refinement, and compressive residual stress. These findings demonstrate that optimizing the laser incidence angle can improve strengthening efficiency and provide an effective strategy for surface modification of critical regions in complex molds.

Keywords: H13 steel; oblique laser shock peening; plasma-nitrided; wear resistance

1. Introduction

The ejection system of precision injection molds is primarily designed to facilitate the smooth demolding of injection-molded components. During the demolding process, repeated sliding contact between the ejector pin and the inner wall of the ejector pin hole inevitably causes friction-induced wear, which may eventually result in dimensional degradation and even premature mold failure under severe conditions. Since injection molds generally require high dimensional accuracy and long service life, the wear resistance of critical friction-contact regions plays a decisive role in determining their reliability. H13 hot-work tool steel exhibits excellent hardenability, strength, toughness, and thermal stability and is widely used in the fabrication of precision injection molds, die-casting molds, and extrusion dies [1–4]. Therefore, developing effective surface strengthening strategies to improve the wear resistance of H13 steel, particularly in critical regions subjected to severe friction, is of great importance for extending mold service life and improving manufacturing reliability.

Check for updates

Academic Editor: Angela De Bonis

Received: 15 June 2026
Revised: 15 July 2026
Accepted: 16 July 2026
Published: 21 July 2026

To improve the wear resistance of H13 steel, various surface modification techniques have been developed, including cryogenic treatment, carburizing, plasma nitriding, surface coating, and laser cladding. Ridvan [5] improved the wear resistance of H13 steel through cryogenic treatment by promoting martensitic transformation and the precipitation of fine carbides. Divagar [6] applied a liquid carburizing treatment to H13 steel and formed a carburized layer on the surface, increasing the hardness from 28 HRC to 55 HRC and significantly reducing the wear rate. Fernandes [7] reported that plasma nitriding effectively reduced the friction coefficient of H13 steel by forming a high-hardness nitrided layer. In addition, coating technologies and laser cladding methods have also been widely employed to enhance surface wear resistance. However, insufficient interfacial bonding strength between coatings and substrates may result in coating delamination during service [8], while excessively high coating hardness may induce brittle cracking [9]. Furthermore, the thermal effects associated with laser cladding can introduce considerable tensile residual stresses, which negatively affect long-term wear performance [10].

Although these approaches can effectively improve the wear resistance of external surfaces, their effectiveness remains limited for complex internal regions, such as deep holes, narrow channels, and curved inner surfaces commonly found in advanced mold components. On one hand, conventional thermochemical treatments and coating technologies often suffer from difficulties in achieving uniform modification on confined inner surfaces. On the other hand, mechanical surface strengthening techniques can introduce plastic deformation, work hardening, and compressive residual stresses, but their applications are restricted by tool accessibility and geometric limitations. Miao [11] strengthened internal threads of high-strength steel through cold extrusion and found that grain refinement and compressive residual stress generation significantly improved fatigue performance. Dang [12] applied ultrasonic rolling to 300 M steel and demonstrated that the increased surface hardness and optimized residual stress state effectively enhanced wear resistance. Zhang [13] strengthened 7075 aluminum alloy using water jet treatment and found that enhanced surface plastic deformation increased hardness and compressive residual stress, thereby improving surface properties. However, these techniques still exhibit limitations for small-hole strengthening. For example, ultrasonic rolling equipment generally suffers from limited accessibility due to its large size [14]; excessive deformation during cold extrusion may induce surface cracking, particularly for hardened materials [15–17]; and water jet treatment may increase surface roughness, affecting subsequent tribological performance [18]. Therefore, developing an effective surface modification technology capable of strengthening confined regions of complex mold components remains highly desirable.

LSP is an advanced surface modification technology that utilizes high-energy laser-induced shock waves to generate severe plastic deformation, grain refinement, work hardening, and compressive residual stress in metallic materials. Due to these advantages, LSP has been considered a promising approach for improving surface mechanical properties and service performance [19]. Wang [20] investigated the effects of laser shock peening (LSP) on the microstructure and mechanical properties of 7075 aluminum alloy and found that LSP promoted grain refinement and dislocation accumulation, resulting in increased microhardness, tensile strength, and strain-hardening capability. Yin [21] studied the effect of LSP on the impact wear resistance of Ti-6Al-4V alloy and demonstrated that both wear track width and maximum wear depth were significantly reduced after LSP treatment. However, conventional LSP generally requires near-normal laser incidence, which restricts its application on geometrically confined regions, such as deep cavities, narrow grooves, and small-hole inner surfaces, where direct laser access is difficult.

To overcome the limitations of conventional LSP in complex geometries, OLSP has been developed by introducing non-normal laser incidence, enabling more flexible energy

https://doi.org/10.3390/coatings16070874

delivery toward restricted surfaces. Dai [22] found that the plastically affected depth increases with increasing laser spot diameter. Lin [23] applied OLSP to aircraft engine turbine disk tenon structures and found that both surface hardness and compressive residual stress were significantly improved. They further demonstrated that the incident angle strongly influenced the induced compressive residual stress, surface roughness, and microhardness. Li [24] conducted orthogonal experiments on FGH95 superalloy using OLSP with a 30° incident angle and determined optimized processing parameters of 8 J laser energy and a 3 mm beam diameter. Under these conditions, the microhardness increased by 24.56%, while the magnitude of surface compressive residual stress increased by 17.47%.

In practical mold manufacturing, complex structures such as deep cavities, narrow holes, and curved surfaces are frequently encountered, creating significant challenges for conventional surface strengthening technologies. The flexible energy delivery capability of OLSP provides potential advantages for modifying these geometrically restricted regions. Moreover, the compatibility of OLSP with automated laser systems, multi-axis processing platforms, and robotic manufacturing technologies provides opportunities for industrial-scale application in advanced mold surface modification. However, several challenges remain for the practical implementation of OLSP. The oblique incidence configuration may reduce laser energy coupling efficiency and shock pressure transmission, resulting in reduced strengthening effectiveness and non-uniform residual stress distributions. In addition, precise control of processing parameters, including incident angle, laser energy density, and scanning strategy, is essential to achieve reliable strengthening effects on complex three-dimensional surfaces. Therefore, understanding the relationship between laser incidence angle, microstructural evolution, residual stress generation, and tribological performance is critical for the further development of OLSP-based surface engineering technologies.

For the strengthening requirements of small-hole inner surfaces and other confined regions, a single OLSP process may not be sufficient to simultaneously achieve high hardness, large compressive residual stress, and stable microstructural characteristics. Plasma nitriding can provide a high-hardness diffusion layer and improve the load-bearing capability of the surface, whereas OLSP can further induce severe plastic deformation, grain refinement, dislocation accumulation, and compressive residual stress generation. Therefore, combining plasma nitriding with OLSP is expected to construct a multifunctional gradient strengthening layer characterized by hardness gradient, microstructural gradient, and residual stress gradient, thereby achieving synergistic improvement in the wear resistance of complex mold components.

Based on this consideration, this study proposes a combined plasma nitriding and OLSP surface modification strategy for improving the service performance of H13 steel. The effects of the combined treatment on microstructural evolution, microhardness distribution, residual stress profile, and tribological behavior were systematically investigated. Furthermore, the influence of laser incidence angle on the strengthening effectiveness was analyzed, and the synergistic strengthening mechanism responsible for the enhanced wear resistance was revealed through comprehensive analysis of wear morphology and quantitative wear parameters. This work provides theoretical insights and technical guidance for the surface strengthening of high-performance mold components with complex geometries.

2. Materials and Methods

2.1. Experimental Materials

The material investigated in this study was H13 steel. Since no standardized testing equipment is currently available to directly simulate wear behavior inside ejector pin

https://doi.org/10.3390/coatings16070874

holes, a conventional wear test was employed to evaluate the tribological properties of the material. The chemical composition of the H13 steel is listed in Table 1. For the initial heat treatment process, the specimens were subjected to a two-stage preheating treatment: first heated to 450–500 °C and held for 30 min, followed by heating to 800–850 °C and holding for 30 min to ensure uniform temperature distribution and preliminary homogenization. Subsequently, the samples were austenitized at 1050 °C for 45 min in a muffle furnace and quenched in oil at room temperature (approximately 60–80 °C). After quenching, a double tempering treatment was performed at 500 °C for 2 h each cycle, followed by air cooling to room temperature. As shown in Figure 1, Ø40 mm × 10 mm (diameter × thickness) circular samples were made through wire cutting and then ground to a surface roughness of Ra0.8 using a surface grinder. The sample surfaces were ground and polished, cleaned with ethanol, dried, and then stored for subsequent testing.

Table 1. Chemical composition (wt%) of the H13 steel.

Element	C	Si	Mn	Cr	Mo	V	S	P
wt%	0.46	1.10	0.39	4.90	1.21	0.88	0.004	0.011

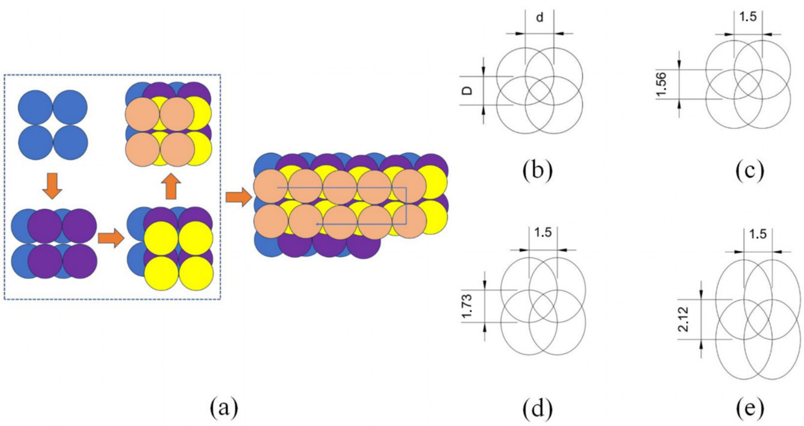

Figure 1. Laser shock path and spot bonding scheme (**a**,**b**), angle 15° (**c**), angle 30° (**d**), angle 45° (**e**).

2.2. Plasma Nitriding Experiment

The plasma nitriding treatment was performed in an LDNBMC-F vacuum plasma-nitriding furnace (Wuhan Heat Treatment, Wuhan, China) at 480 °C for 8 h under a controlled N_2:H_2 gas mixture of 450 mL/min:150 mL/min. The chamber pressure was maintained at 400 Pa throughout the process. A pulsed DC voltage of 520–580 V was applied, and the current density was controlled at approximately 2.5–3.0 mA/cm^2 to sustain a stable plasma state and promote uniform nitrogen diffusion. After plasma nitriding, all specimens were furnace-cooled to room temperature.

2.3. Laser Shock Peening

The LSP process is a physical surface modification technique based on the interaction between a high-power-density nanosecond pulsed laser and the target material. It utilizes the mechanical effects induced by laser-generated shock waves to modify the material surface. During laser shock processing, the water confinement layer restricts plasma expansion, thereby increasing the pressure of the generated shock wave. When a high-energy laser pulse irradiates the material surface, the sacrificial absorption layer is instantaneously melted and vaporized, producing high-temperature and high-pressure plasma. The plasma subsequently absorbs additional laser energy and undergoes rapid expansion. Due to the confinement effect of the water layer, the free expansion of the plasma is suppressed, resulting in the generation of a high-pressure shock wave that propagates into the material and induces plastic deformation [25].

The relationship between laser power density and plasma shock wave pressure peak proposed by Fabbro [26]:

$$P = 0.1\left(\frac{\alpha}{2\alpha+3}\right)^{0.5} Z^{0.5} I^{0.5} \tag{1}$$

$$\frac{2}{Z} = \frac{1}{Z_1} + \frac{1}{Z_2} \tag{2}$$

where $P(t)$ is the peak pressure of the shock wave, unit: Kbars; α is the internal energy conversion coefficient, with a value of $\alpha = 0.2$; Z is the acoustic impedance, unit: $g{\cdot}cm^{-2}{\cdot}s^{-1}$; and I represents the laser power density, unit: $GW{\cdot}cm^{-2}$. The acoustic impedance of the water confinement layer is $Z_1 = 1.65 \times 10^5\ g \cdot cm^{-2} \cdot s^{-1}$, while the acoustic impedance of the H13 steel substrate is [27] $Z_2 \approx 4.57 \times 10^6\ g \cdot cm^{-2} \cdot s^{-1}$. Substituting Z_1 and Z_2 into Equation (2), the effective acoustic impedance of the water–H13 steel system is calculated as $Z = 3.19 \times 10^5\ g \cdot cm^{-2} \cdot s^{-1}$.

Therefore, combining Equations (1) and (2), the relationship between the laser power density and the shock wave pressure can be simplified as:

$$P = 1.5\sqrt{I} \tag{3}$$

The high-pressure shock wave generated by laser irradiation induces localized stress concentration on the metallic surface. Under one-dimensional strain loading conditions, the normal stress corresponding to the onset of plastic deformation is defined as the Hugoniot elastic limit (HEL) of the material [28].

$$\sigma_{HEL} = \left(\frac{K}{2G} + \frac{2}{3}\right)\gamma_0 \tag{4}$$

$$K = \frac{E}{3(1-2v)} \tag{5}$$

$$G = \frac{E}{2(1+v)} \tag{6}$$

where K is the bulk modulus, unit: GPa; G is the shear modulus, unit: GPa; E is the elastic modulus, unit: GPa; ν is Poisson's ratio, unit: dimensionless; and γ_0 represents the yield strength of the material, unit: GPa. By substituting Equations (4)–(6), the Hugoniot elastic limit (HEL) can be simplified as:

$$\sigma_{HEL} = \frac{1-\nu}{1-2\nu}\gamma_0 \tag{7}$$

According to the material handbook, the Poisson's ratio of H13 steel is $\nu = 0.31$, and the yield strength is approximately $\gamma_0 \approx 1300$ MPa. Therefore, the calculated HEL value of H13 steel is approximately 2.3 GPa. When the shock pressure exceeds the HEL, plastic deformation occurs. By substituting σ_{HEL} into Equation (3), the critical laser power density required to induce plastic deformation can be determined as: $I_0 = 2.35\ GW/cm^2$.

Furthermore, the optimal shock-strengthening effect can be obtained when the shock pressure satisfies $2\sigma_{HEL} < P < 2.5\sigma_{HEL}$. For H13 steel, this corresponds to:

$$4.7 \ < P \ < \ 5.875 \ \ GW/cm^2 \tag{8}$$

By combining Equations (3) and (8), the optimal laser power density range for LSP was determined to be $9.8 < I < 15.3\ GW/cm^2$. However, when the laser power density exceeds 10 GW/cm^2, the laser energy may be partially attenuated due to the breakdown of the water confinement medium, resulting in reduced energy transfer efficiency to the target material. Therefore, although the theoretically predicted optimal power density falls within the range of $9.8 < I < 15.3$ GW/cm^2, a laser power density of 10 GW/cm^2 was selected in this study considering the stability of laser energy transmission and experimental feasibility.

LSP experiments were conducted using a TYRIDA Lamber-12 laser system (TYRIDA LAMBER, Xi'an, China). Considering the dimensional characteristics of the ejector pin holes and their actual service conditions, the laser pulse duration was set to τ = 20 ns, and the spot overlap rate was maintained at 50%. When the laser incidence angle was varied within the range of 15–45°, the laser shock peening region could effectively reach approximately 8 mm in depth inside the hole, thereby covering the primary wear-affected region during service. Therefore, three representative incidence angles of 15°, 30°, and 45° were selected as experimental variables to investigate their effects on the strengthening efficiency. The corresponding laser spot diameters under these three incidence angles were calculated, as shown in Figure 2. The laser spot area was subsequently determined using the following equation:

$$S = \pi ab \tag{9}$$

where a is the major axis radius and b is the minor axis radius.

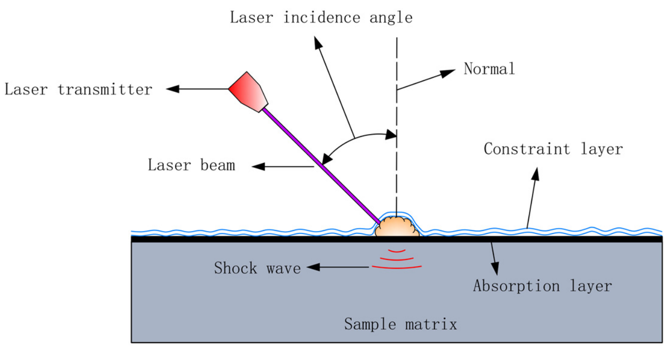

Figure 2. Principles of OLSP.

When the laser is vertically impacted, the relationship between the laser energy and the spot area of the laser power densitometer is shown in Formula (10) [23]:

$$E = I_0 \tau S \tag{10}$$

According to Equations (9) and (10), the required laser energy is calculated to be within the range of $7.35 < E < 9.99$ J. Therefore, a laser energy of 8 J was selected for the LSP experiments.

Using the TYRIDA LAMBER-12 laser, which is equipped with Q-switching technology and utilizes Nd:YAG (neodymium-doped yttrium aluminum garnet) laser oblique impact experiments were conducted, with its principle and process parameters shown in Figure 2 and Table 2, respectively. The laser had a wavelength of 1064 nm and a laser pulse duration of 20 ns. Use 0.1 mm thick PVC black tape as the absorption layer. To achieve a greater stress amplitude and duration, 2 mm thick flowing water was used as the constraint layer. The spot diameter, overlap rate, and pulse energy were 3 mm, 50%, and 8 J, respectively. The laser shock path and spot overlap scheme are shown in Figure 1. A 50% overlap of the spots is achieved through four sets of laser impacts. After each set of experiments, a new black tape is used for the next set of experiments until the end of the experiment.

Table 2. LSP process parameters.

Type	Value
Spot diameter (mm)	3
Laser pulse energy (J)	8
Laser wavelength (nm)	1064
Laser incidence angle	15°, 30°, 45°
Overlap rate	50%

At a constant laser pulse energy of 8 J, only the laser incidence angle was varied in order to systematically investigate its effect on the strengthening performance. Therefore, as shown in Table 3, laser incidence angles of 15°, 30°, and 45° were selected, and all samples were labeled. The experimental group consists of 5 groups with 3 samples in each group, and all sample groups are labeled, as shown in Table 3.

Table 3. Sample numbers for different process parameters.

Sample Number	Technological Parameter
Untreated	Unprocessed
Plasma-nitrided	Plasma nitriding technology
NLSP1	Plasma nitriding technology and LSP (energy 8 J, angle 15°)
NLSP2	Plasma nitriding technology and LSP (energy 8 J, angle 30°)
NLSP3	Plasma nitriding technology and LSP (energy 8 J, angle 45°)

2.4. Friction and Wear Test

Friction and wear tests were performed using a UMT-2 CETR friction and wear tester (Bruker, CETR, Billerica, MA, USA). A ball-on-disk (BOD) configuration was adopted to evaluate the wear resistance of the samples, and all experiments were conducted strictly according to the ASTM G99-23 standard (Standard Test Method for Wear and Friction Testing with a Pin-on-Disk or Ball-on-Disk Apparatus). A 10 mm diameter ball coated with cubic boron nitride (CBN) was selected as the counterbody. The rotation radius, applied load, rotation speed, and wear duration were set to 10 mm, 20 N, 250 r/min, and 1 h, respectively. The detailed wear test procedure is illustrated in Figure 3. Each experimental condition was tested once, and the wear characteristics were analyzed based on the obtained wear tracks.

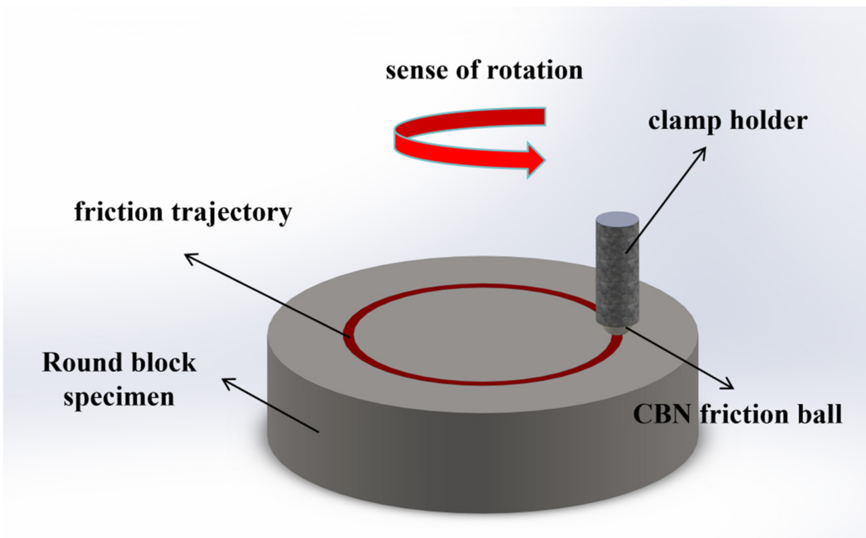

Figure 3. BOD wear test.

2.5. Observation of Surface Microstructure

To study the effects of different processes on the microstructure of H13 steel, samples treated with different processes were cut into blocks through wire cutting before being ground and polished, cleaned, and then corroded with 4% nitric acid alcohol. After cleaning the surface, the metallographic surface structures of the samples were observed using a Keyence VK-X100 confocal laser microscope (Keyence, Osaka, Japan). A Bruker D8 Focus multifunctional diffractometer was used for X-ray diffraction analysis (XRD) of the samples, enabling phase analysis of the material. The working voltage, current, target material, scanning range, and scanning speed were 35 KV, 40 mA, Co-Kα target, 10~110°, and 2°/min, respectively. To characterize the microstructure of the processed sample surface layers, an electron backscatter diffraction (EBSD) analysis was conducted using high-resolution scanning electron microscopy (EDAX Velocity Super, Mahwah, NJ, USA). This analysis aimed to capture changes in crystal orientation, grain plastic deformation, grain size, local orientation differences, and inverse pole figures (IPFs) of the samples.

2.6. Microhardness

At a test load of 0.1 kg^{-f}/mm^{-2} and a duration of 10 s, the surface microhardness of the samples was characterized using a FALCON500 Vickers hardness tester (INNO VATEST Shanghai Co. Ltd., Shanghai, China). The material was tested in both the surface and cross-sectional depth directions at each measurement location, with each data point representing the average of three measured results.

2.7. Residual Stress

A Proto iXRD high-speed residual stress analyzer (Proto, LaSalle, Canada) was used to characterize the residual stress of the samples based on the $\sin^2\psi$ method. This method is based on the principle that residual stresses induce elastic lattice deformation, resulting in variations in interplanar spacing and corresponding shifts in diffraction peak positions. By measuring the diffraction angle changes in the {211} crystallographic planes at different ψ angles, the lattice strain–$\sin^2\psi$ relationship was established, and the surface residual stress was determined according to the elastic deformation relationship. The residual stress can be calculated according to the following equation:

$$\sigma_{\Phi} = \frac{E}{1+\nu}\frac{d\varepsilon_{\psi}}{d\left(\sin^2\psi\right)} \tag{11}$$

where σ_{Φ} is the residual stress, unit: MPa; E is the elastic modulus, unit: GPa; ν is Poisson's ratio; ε_{ψ} represents the lattice strain at different ψ angles; and $d\left(\sin^2\psi\right)$ is the slope of the linear fitting curve between lattice strain and $sin2\psi$.

The instrument was calibrated using a stress-free [iron] powder standard. The radiation source, V filter/collimator diameter, and diffraction surface were Cr-Kα, 3 mm, and {211}, respectively, and the diffraction angle (2θ) was between 137° and 144°. Measurements were conducted at 9 ψ angles ranging from −45° to +45°, with an effective X-ray penetration depth of approximately 5.5 μm. A saturated NaCl solution was used for electropolishing, which removed the material layer by layer. The average value of the three measurements was taken as the experimental data. The measurement uncertainty was evaluated based on the deviation among the three repeated measurements, and the average residual stress value was reported as the final experimental result.

2.8. Wear Topography

A ZEISS LSM900 confocal laser microscope (Zeiss, Oberkochen, Germany) was used to capture the circular wear track of the wear samples and extract the deepest wear data. Three randomly selected positions along each wear track were used to measure the wear depth and width. A ZEISS Crossbeam 550 focused ion beam scanning electron microscope (Zeiss, Oberkochen, Germany) was used to observe the microscopic topography and elemental distribution of the wear surfaces after the wear test, with magnifications of 100 and 1 K, respectively.

To provide a clear overview of the experimental procedure, the entire workflow, including specimen preparation, plasma nitriding treatment, oblique laser shock peening (OLSP) processing, and subsequent characterization and tribological evaluations, is summarized schematically in Figure 4.

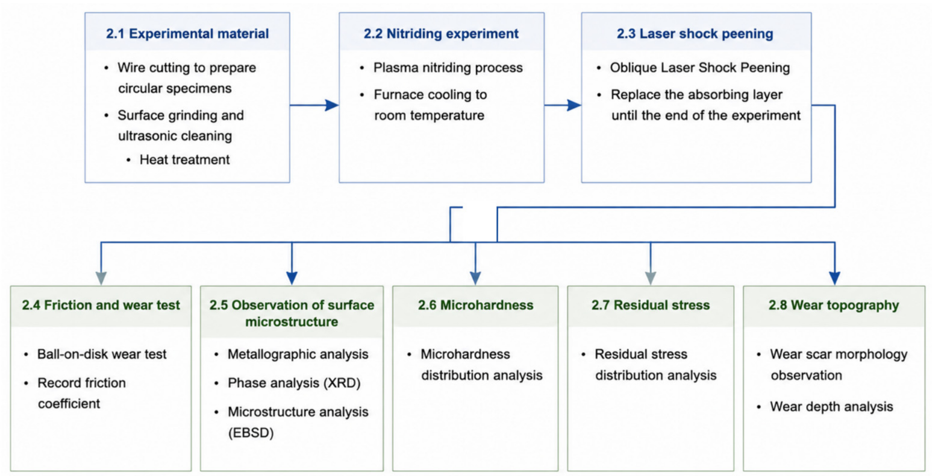

Figure 4. Schematic overview of the complete experimental procedure.

3. Results

3.1. Metallographic Superficial Microstructure Observation and XRD Microstructure Characterization

Figure 5a,b show the microstructures of untreated and plasma-nitrided samples, respectively. The microstructure of the untreated sample is tempered martensite [29], whereas the plasma-nitrided sample exhibits a dark needle-shaped nitride diffusion zone of about 70 μm on the surface layer without any white compound layer.

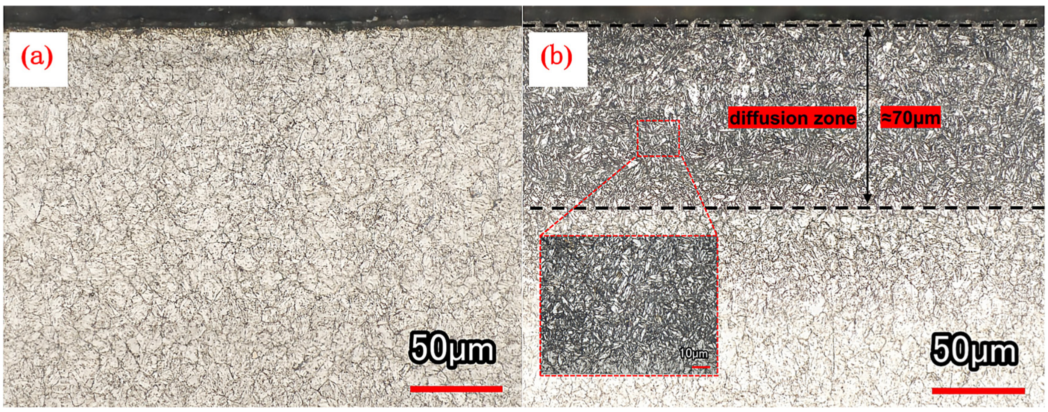

Figure 5. Microstructure of (**a**) untreated sample and (**b**) plasma-nitrided sample.

Figure 6 shows the X-ray diffraction patterns of the untreated and plasma-nitrided samples. The diffraction pattern of the untreated sample has an Fe phase peak, with no diffraction peaks of other compounds present. After plasma nitriding treatment, diffraction peaks of Fe_3N, Fe_4N and nitrogen-containing martensite α' can be clearly detected in the samples. These findings are consistent with the metallographic results shown in Figure 4.

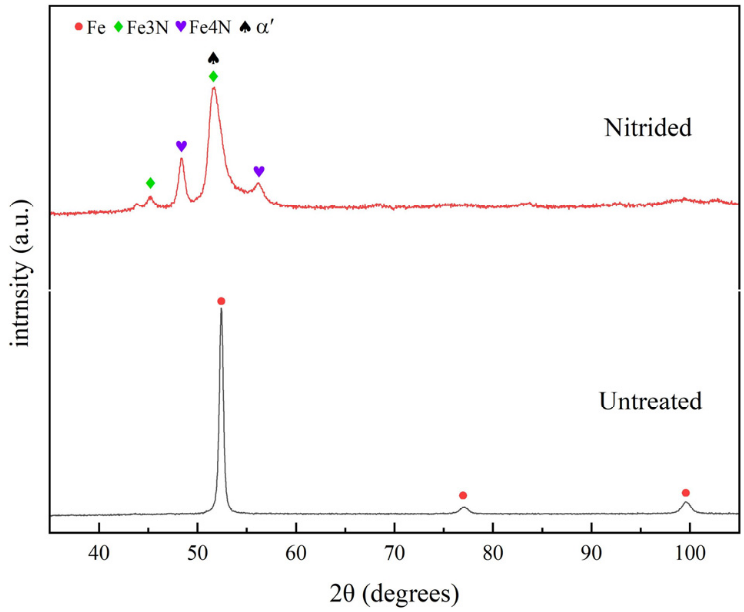

Figure 6. X-ray diffraction of untreated sample and plasma-nitrided sample.

3.2. Microhardness Distribution

Figure 7 shows the cross-sectional microhardness distribution of a sample. Plasma nitriding increases the surface nitrogen content of the plasma-nitrided sample. Once the solubility reaches saturation, nitride is precipitated, and after plasma nitriding, the surface hardness increases significantly. The surface microhardness increases from 544 $HV_{0.1}$ to 1205 $HV_{0.1}$. Comparing the plasma-nitrided sample with the NLSP3 sample, the microhardness of the sample can be further improved after LSP. The surface microhardness of the NLSP3 sample is 1241 $HV_{0.1}$, an increase of 2.99%. As the laser incidence angle decreases, the surface microhardness increases. The surface microhardness of NLSP1 is 1334 $HV_{0.1}$, an increase of 7.49% compared to that of the NLSP3 sample. From the microhardness distribution, the microhardness of the plasma-nitrided sample decreases rapidly at a depth of 70 µm, so it can be estimated that the depth of the effective diffusion zone is about 70 µm. This is consistent with the conclusion obtained in Figure 5b.

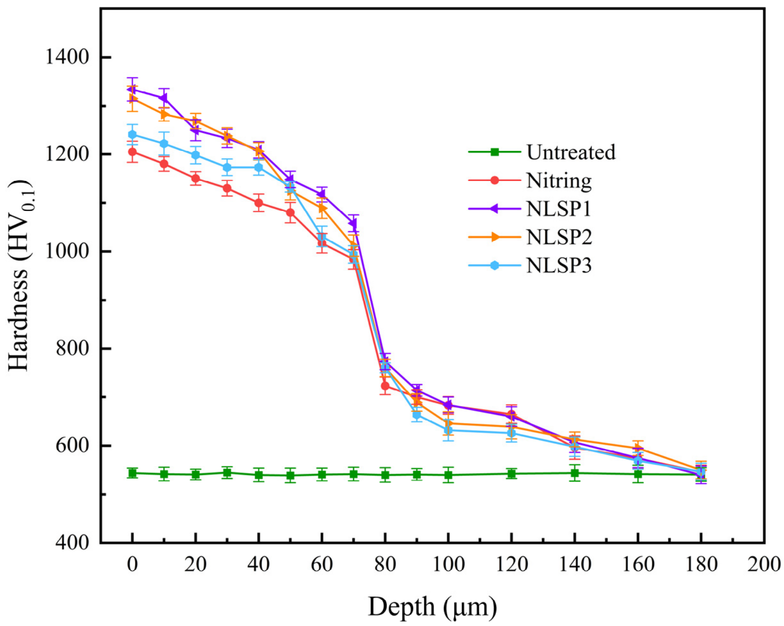

Figure 7. Cross-sectional microhardness distribution.

3.3. Residual Stress Distribution

Figure 8 shows the distribution of residual stress on sample surfaces after different processes. Mechanical grinding on an untreated sample's surface can produce a residual stress of −537 MPa. The maximum residual stress of the plasma-nitrided sample is −686 MPa. The increase in residual stress compared to the untreated sample is due to the nitrogen atoms diffusing into the surface layer of the material to form a plasma-nitrided layer. This process causes changes in the structure of the surface layer of the material, resulting in higher residual stress [30]. The maximum residual stress observed on an NLSP1 sample is −1033 MPa. As the laser incidence angle changes to 30° and 45°, the residual stress decreases to −898 MPa and −884 MPa, respectively. From a depth perspective, the residual compressive stress gradually decreases with increasing depth. This is because as the shock wave propagates into the material, kinetic energy dissipates. The shock wave pressure decreases with increasing depth, resulting in lower internal residual stress [31].

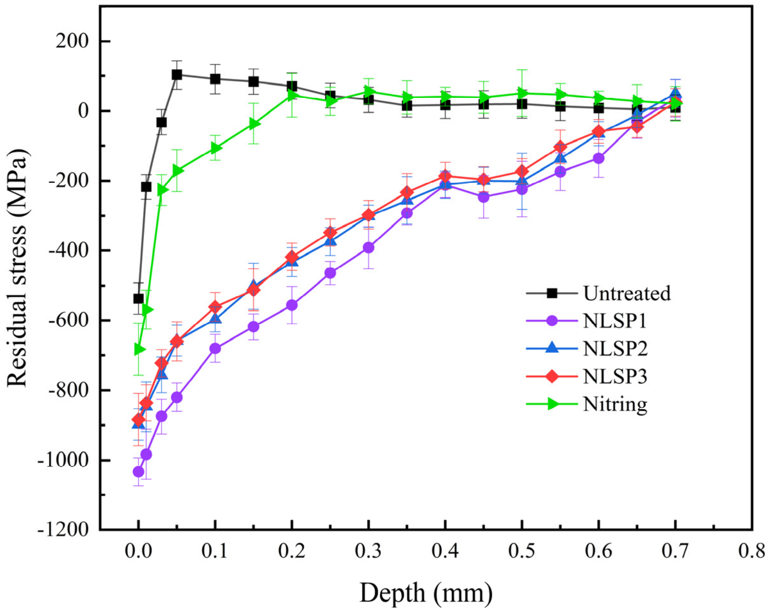

Figure 8. Residual surface stress distribution.

The underlying mechanism for the aforementioned reduction in residual stress during oblique incidence is mainly attributed to energy attenuation and shockwave decomposition. When the laser is obliquely incident at an angle θ, the originally circular laser spot is stretched into a long ellipse on the material surface, increasing its interaction area to 1/cos θ times that of normal incidence. This results in the attenuation of the actual effective power density to $I = I_0 \cos \theta$. Meanwhile, the angle between the plasma expansion direction and the optical axis causes the shock wavefront to deflect and distort. Consequently, the shock wave energy penetrating the material decomposes into longitudinal waves (compressive waves), which drive the deep volumetric plastic strain, and transverse waves (shear waves), which aggravate the lateral plastic flow of the surface layer. As the laser incident angle θ increases, the effective energy allocated to the longitudinal shock wave continuously diminishes, leading to a decreased shock wave loading effect. Therefore, the maximum residual compressive stress induced by NLSP1 is significantly higher than that at other oblique angles.

3.4. EBSD Microstructure Characterization

According to Figures 7 and 8, the samples treated through different processes indicate that NLSP1 has the highest microhardness and residual stress. Therefore, untreated and

NLSP1 samples were selected for EBSD analysis. Figures 9 and 10 show the cross-sectional microstructures of the untreated and NLSP1 samples. Figure 9a,b show the cross-sectional grain distribution of untreated and NLSP1 sample surfaces.

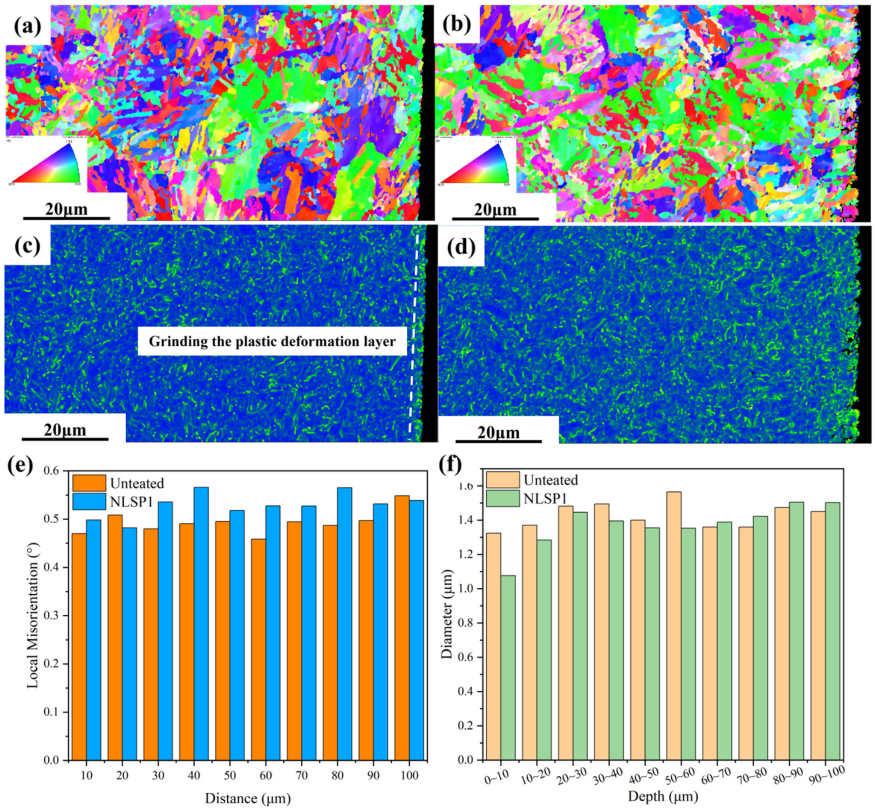

Figure 9. Crystal orientation maps of (**a**) Untreated and (**b**) NLSP1 samples. Local misorientation average angle distribution of (**c**) untreated and (**d**) NLSP1 samples. (**e**) Grain angle comparison at different depths. (**f**) Average grain size at different depths.

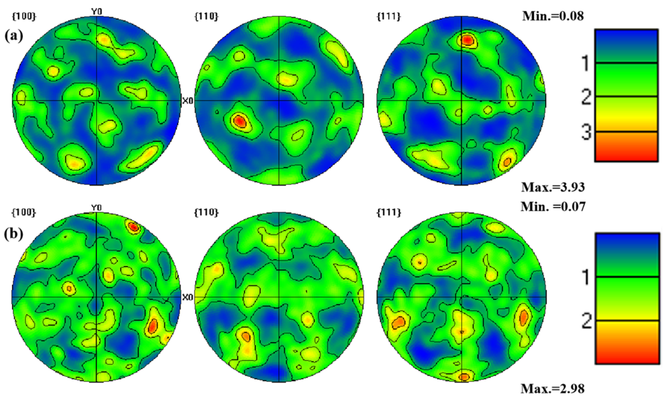

Figure 10. Pole figures of (**a**) untreated and (**b**) NLSP1.

Figure 9c,d show the kernel average misorientation (KAM) maps of the untreated and NLSP1 samples. The local plastic deformation can be assessed through the KAM distribution, where blue indicates local low-angle orientation differences while green indicates local high-angle orientation differences. According to Figure 9c, a 1–2 μm thin plastic deformation layer can be found on the surface of the untreated sample after grinding. According to Figure 9d, the local high-angle orientation difference in an NLSP1 sample surface increases significantly. Figure 9e shows the distribution of grain angles in the depth direction, revealing that the plastic deformation of the NLSP1 sample is more pronounced than that of the untreated sample. Figure 9f shows the average grain size of an NLSP1 sample at different depths. It can be found that the average grain size of 0–10 μm on the surface layer of the NLSP1 sample decreased significantly by 18.7%, compared to that of an untreated sample. This indicates that the surface layer of the NLSP1 sample exhibits more pronounced grain refinement because plastic deformation can help refine the grains. Similar results can also be obtained through other plastic deformation methods for preparing nanocrystalline materials [32].

Figure 10a,b show the IPFs, indicating that the untreated sample has a lower texture density and a higher matrix density. In contrast, the NLSP1 sample exhibits a significantly decreased matrix density, indicating that LSP can disrupt the initial grain orientation and result in a more even grain distribution [33].

3.5. Surface Roughness

The surface roughness of the untreated sample is 0.21, the plasma-nitrided sample is 0.25, the NLSP1 sample is 0.28, the NLSP2 sample is 0.28, and the NLSP3 sample is 0.27. Compared to the untreated sample, the surface roughness of the plasma-nitrided and NLSP1 samples increased by approximately 19.0% and 33.3%, respectively. During plasma nitriding, the material surface is subjected to continuous high-energy ion bombardment, causing a micro-sputtering effect and local topographical changes that slightly increase the roughness. For the NLSP samples, the overlapping of laser spots leaves macroscopic micro-dimples and uneven plastic flow on the surface, which inevitably leads to a more pronounced increase in surface roughness.

3.6. Wear Resistance Characterization

Figure 11 presents the friction coefficient curves of different samples. All samples exhibit pronounced fluctuations in the friction coefficient during the initial sliding stage, which can be attributed to the running-in process between the cubic boron nitride counterbody and the sample surfaces. During this stage, a higher surface roughness promotes asperity interaction and increases the real contact area, resulting in enhanced mechanical interlocking and unstable friction fluctuations. With continuous sliding, the progressive removal of surface asperities and the formation of a relatively stable tribofilm contribute to the stabilization of the friction coefficient.

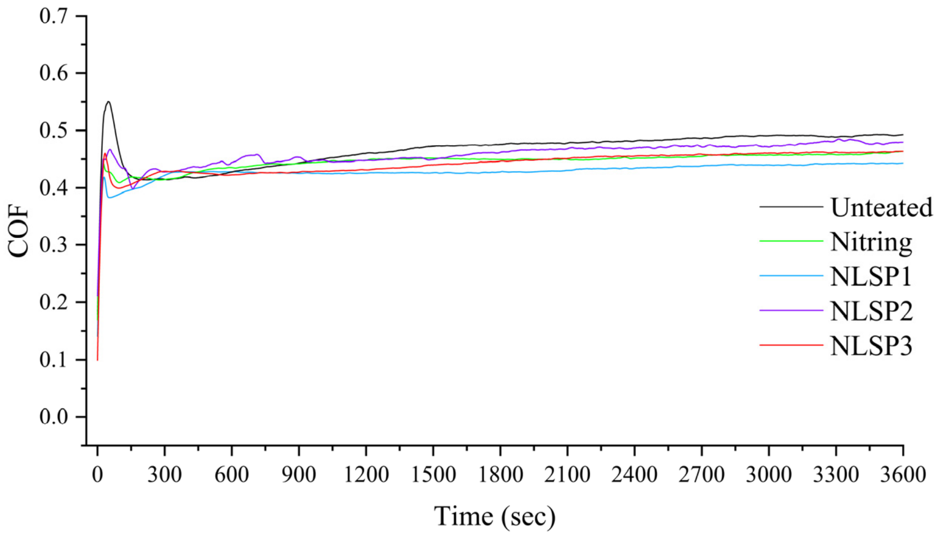

Figure 11. Friction coefficient curve.

After 3600 s of wear testing, the average friction coefficients of the untreated, plasma-nitrided, and NLSP1 samples were 0.48, 0.44, and 0.42, respectively. Compared with the

https://doi.org/10.3390/coatings16070874

untreated sample, the plasma-nitrided sample exhibited a reduced friction coefficient, which can be attributed to the formation of a high-hardness nitrided layer that effectively improves resistance against counterbody penetration and suppresses severe plastic deformation during sliding. Furthermore, the NLSP1 sample exhibited the lowest and most stable friction coefficient. This improvement is mainly associated with the high-magnitude compressive residual stresses introduced by LSP, which effectively suppress crack initiation and propagation during sliding wear. Consequently, material delamination and subsequent third-body abrasive wear are mitigated, leading to reduced friction fluctuations and enhanced tribological stability [34].

Figure 12 shows the wear morphology and cross-sectional profile of the average wear track. According to Figure 12a, the wear scar width and wear depth on the untreated sample are 634.18 µm and 2.55 µm, respectively. After plasma nitriding, the wear scar width and wear depth on the plasma-nitrided sample are 537.12 µm and 1.83 µm, respectively. However, compared to the plasma-nitrided sample, the wear scar width and wear depth on the NLSP sample decrease further after LSP treatment. The wear scar width and wear depth on the NLSP1 sample are the lowest, measuring 523.52 µm and 1.41 µm, respectively. The NLSP process can reduce the wear scar width and wear depth by 17% and 45%, respectively. However, according to Figure 12f–h, the wear depth increases slightly with the increase in oblique laser angle.

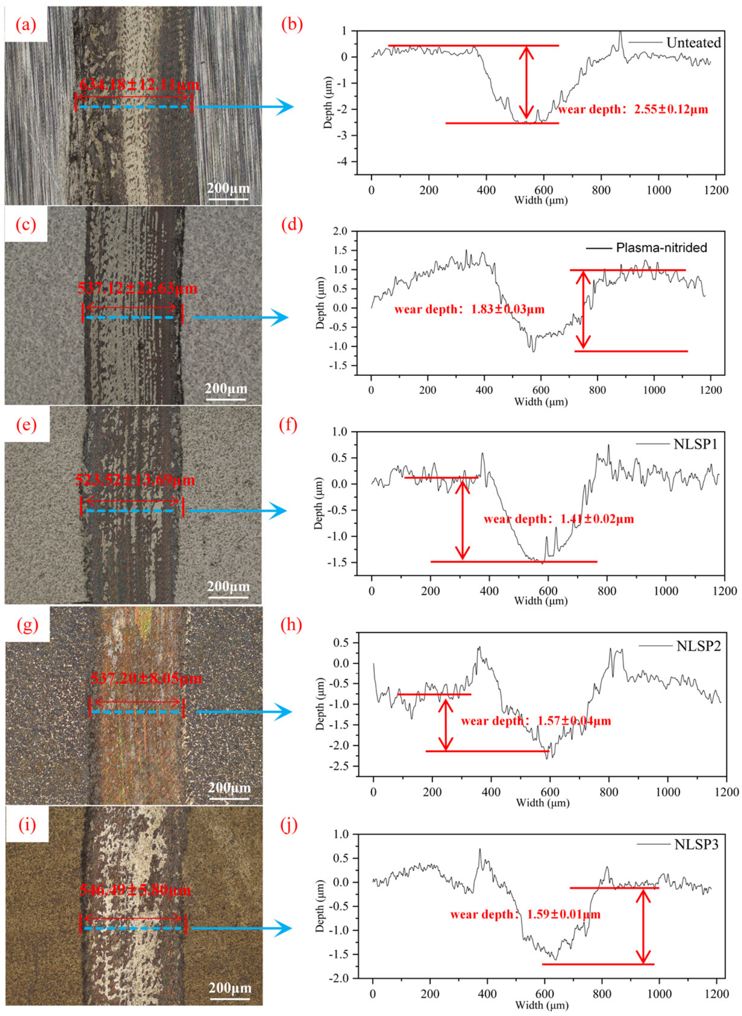

Figure 12. Wear morphology and cross-sectional profile of the average wear track: (**a**,**b**) untreated, (**c**,**d**) plasma-nitrided, (**e**,**f**) NLSP1, (**g**,**h**) NLSP2, (**i**,**j**) NLSP3.

As shown in Figure 13a,b, three randomly selected regions along each wear track were analyzed to ensure the reliability of wear parameter characterization. The maximum wear depth and wear track width were extracted from the cross-sectional profiles of these regions, and the averaged values were adopted as representative wear parameters for each specimen. Subsequently, the wear volume [35] and specific wear rate were calculated to quantitatively evaluate the wear behavior of specimens subjected to different surface treatments, with the corresponding results shown in Figure 13c,d.

$$V_W = \frac{2\pi \mathrm{rt}}{6b}\left(3t^2 + 4b^2\right) \tag{12}$$

where r denotes the wear track radius, unit: mm; t represents wear depth, unit: µm; and b represents wear track width, unit: µm.

$$K = \frac{V}{F \times L} \tag{13}$$

where V represents the wear volume, unit: mm^3; F denotes the applied normal load, unit: N; and L corresponds to the sliding distance, unit: m.

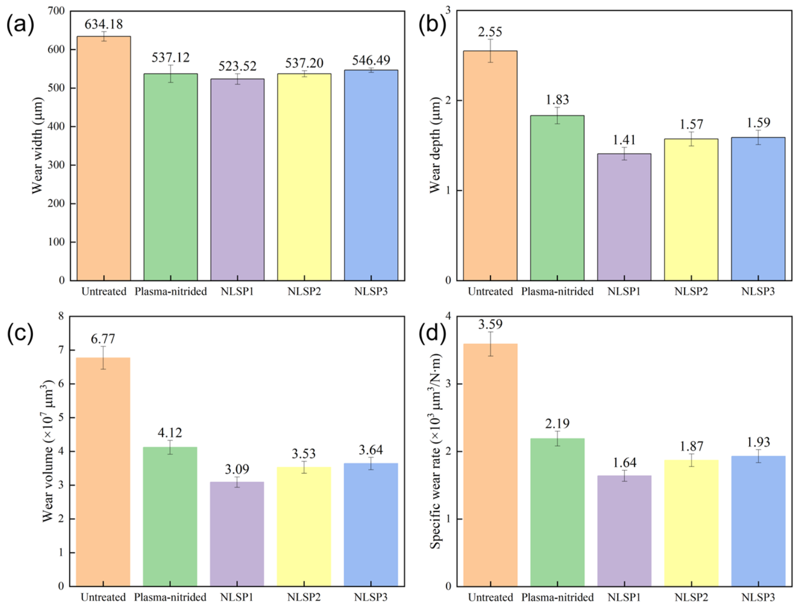

Figure 13. Effect of plasma nitriding and OLSP on the quantitative wear characteristics: (**a**) wear track width, (**b**) wear depth, (**c**) wear volume, and (**d**) specific wear rate.

As shown in Figure 13a,b, the NLSP1-treated specimen exhibited the lowest average wear depth and average wear track width, with values of 1.41 µm and 523.52 µm, respectively. Compared with the untreated and plasma-nitrided specimens, the wear depth of NLSP1 was reduced by 45% and 17%, while the wear track width decreased by 17% and 3%, respectively. With an increasing laser incidence angle, the wear depth and wear track width of the NLSP2 and NLSP3 specimens were slightly increased compared with those of the NLSP1 specimen.

According to the wear volume results shown in Figure 13c, the wear volumes of plasma-nitrided, NLSP1, NLSP2, and NLSP3 specimens were reduced by 39.1%, 54.7%, 47.8%, and 46.2%, respectively, compared with the untreated specimen. The specific wear rate results in Figure 13d further confirmed the superior wear resistance of the NLSP1 specimen. The specific wear rate of NLSP1 was only 1.64×10^{-6} $mm^3/(N{\cdot}m)$, representing reductions of 54.3% and 25.1% compared with the untreated and plasma-nitrided specimens, respectively. As the laser incidence angle increased, the specific wear rates of NLSP2 and NLSP3 increased compared with NLSP1. Overall, the NLSP1 specimen exhibited the optimal wear resistance among all investigated conditions.

The enhanced wear resistance can be attributed to the synergistic effects of the composite strengthening layer. The high-hardness nitrided layer formed during plasma nitriding improved the load-bearing capacity of the surface and reduced the penetration depth of the counterpart during sliding contact. Meanwhile, the compressive residual stress introduced by LSP mitigated tensile stress concentration under cyclic friction loading, thereby delaying crack initiation and subsurface crack propagation. Furthermore, the composite treatment generated a strengthened layer with coupled hardness, residual stress, and microstructural gradients, which effectively optimized the surface stress distribution and deformation compatibility. Consequently, the improved wear resistance resulted from the combined effects of hardness enhancement, dislocation strengthening, compressive residual stress regulation, and stabilization of heterogeneous microstructures [36].

Figures 14 and 15 show the sample wear surface topographies and energy spectrum analyses. According to Figure 14a,e, the wear trajectories of the untreated sample exhibit zones with different shades. Figure 14b,f are partial enlargements of Figure 14a,b and reveal distinct micro-scratch and micro-cutting mark characteristics on the wear topographies of the untreated and plasma-nitrided samples [37]. By comparing Figure 14c,i,j with Figure 14g,k,l, it can be observed that the lighter-colored zones 2 and 4 mainly correspond with the elemental compositions of H13 steel. Zones 1 and 3, which are dark in color, contain significant amounts of oxygen, indicating that these dark areas are oxides. Figure 15a,e show the wear surface topographies after the NLSP process. According to Figure 15b,f, micro-scratch and micro-cutting mark characteristics still exist on the surfaces, which are essentially similar to the wear characteristics of the untreated sample. Comparing Figure 15c,i,j with Figure 15g,k,l, similar results to those of Figure 14 can be observed. Specifically, Zones 1 and 3, which are light in color in Figure 15, correspond to the H13 matrix, while Zones 2 and 4, which are dark in color, are oxide zones.

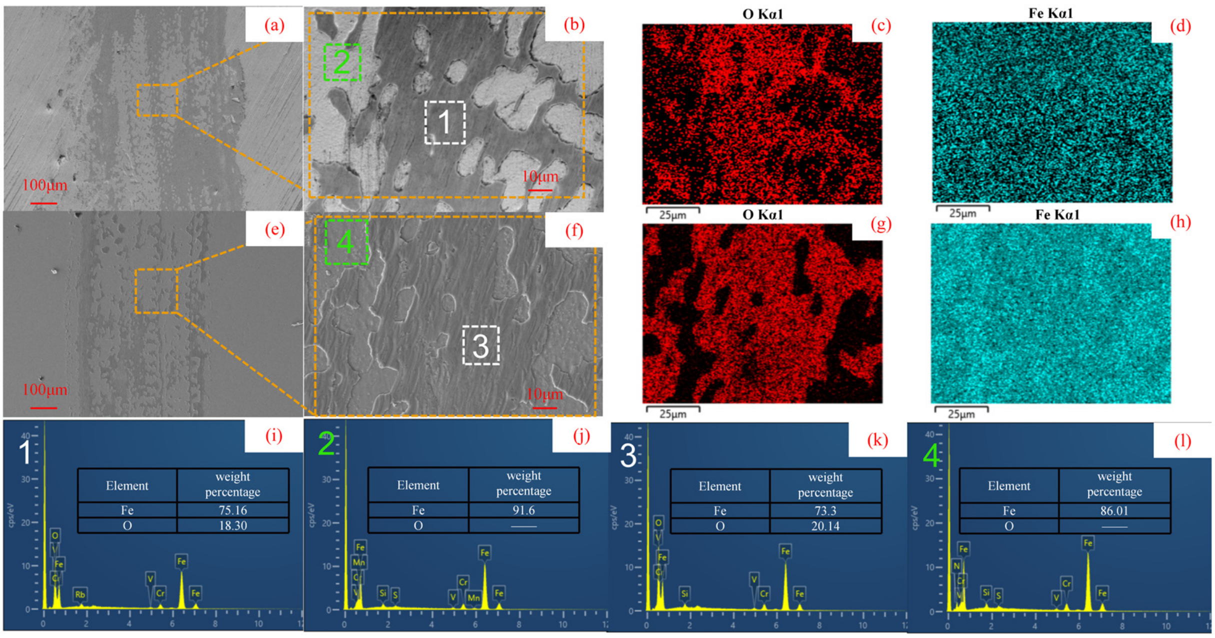

Figure 14. Wear surface topographies and energy spectrum analyses. (**a**,**b**) untreated surface topographies; (**c**,**d**,**i**,**j**) untreated energy spectrum analyses; (**e**,**f**) plasma-nitrided surface topographies; and (**g**,**h**,**k**,**l**) plasma-nitrided energy spectrum analyses.

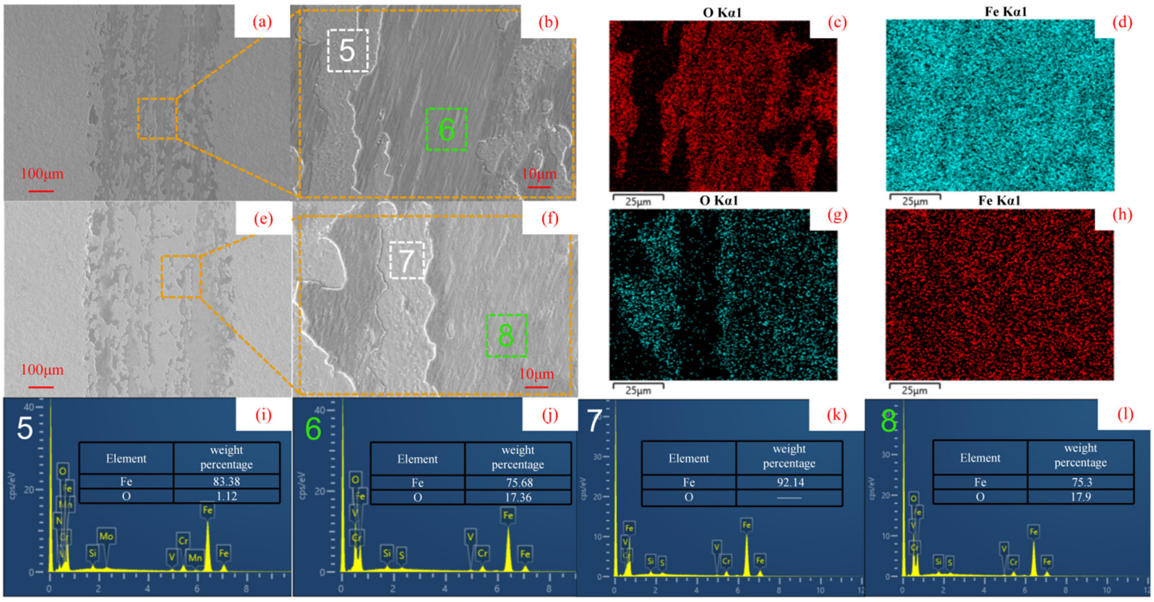

Figure 15. NLSP sample wear surface topographies and energy spectrum analyses. (**a**,**b**,**e**,**f**) NLSP surface topographies; (**c**,**d**,**i**,**j**) and (**g**,**h**,**k**,**l**) energy spectrum analyses.

As shown in Figures 14a and 15e, the untreated specimen exhibited a larger area and larger-sized oxide adhesion on the worn surface compared with the NLSP1 specimen. During the sliding process, a large amount of wear debris generated from the untreated specimen was not effectively removed and was subsequently oxidized, forming oxidized debris. These debris particles acted as third-body abrasives during sliding wear, intensifying the abrasive wear process and accelerating surface material removal. Moreover, the relatively low surface hardness and poor structural stability of the untreated specimen made it more susceptible to plastic deformation and localized spalling under cyclic frictional loading, resulting in the formation of larger wear pits and oxide accumulation.

In contrast, although a small amount of oxide adhesion was still observed on the NLSP1 specimen, the size and distribution of these oxides were significantly reduced. The worn surface mainly exhibited shallow and fine wear grooves with a relatively smooth morphology. This improvement can be attributed to the gradient strengthening layer generated by the combined plasma nitriding and OLSP treatments. The strengthened layer, characterized by enhanced surface hardness and compressive residual stress, improved the resistance of the surface against plastic deformation and reduced the generation of wear debris during sliding. Meanwhile, the gradient hardness structure alleviated deformation incompatibility between the strengthened surface layer and the substrate, facilitating the formation of a stable tribo-compacted layer and reducing the detrimental effect of third-body abrasive particles. Furthermore, the compressive residual stress counteracted the localized tensile stresses generated during friction, thereby suppressing crack initiation and propagation [36].

4. Discussion

As shown in the metallographic superficial microstructure observation results in Figure 4 and the XRD microstructure characterization results in Figure 5, plasma nitriding primarily relies on the solid solution strengthening of N atoms and the dispersion strengthening of nitrides [38,39]. The infiltration of nitrogen atoms can lead to changes in the metal's surface microstructure and near-surface zones, which helps improve the material's hardness [40].

The strengthening mechanism was further analyzed and verified based on the Hall–Petch effect and Taylor strengthening [41]:

$$H_v = H_0 + Kd^{-1/2} + M\alpha Gb\rho^{1/2} \quad (14)$$

where H_V, H_0, and k represent the local hardness, matrix hardness, and Hall-Petch constant, respectively; d, M, and α represent the average grain size, Taylor factor, and material constant, respectively; and G, b, and ρ represent the shear modulus, Burgers vector value, and dislocation density, respectively. According to the combined Hall–Petch and Taylor strengthening model, the hardness enhancement induced by LSP was further quantitatively evaluated. The calculated results indicate that grain refinement contributed approximately 15.2 HV through Hall–Petch strengthening, while dislocation strengthening provided an additional contribution of approximately 88.5 HV based on the Taylor strengthening mechanism. The total strengthening contribution from these two mechanisms was estimated to be approximately 103.7 HV, suggesting that dislocation strengthening played a dominant role in the hardness improvement after LSP.

The microhardness of sample surfaces treated with LSP gradually decreases with an increase in incident angle. This can be explained by the pressure distribution of laser-induced shock waves, which follows a Gaussian load [42]:

$$P(r,t) = P(t)\exp\left(-\frac{r^2}{2R^2}\right) \quad (15)$$

where r represents the center distance of a laser spot projected onto a metal plate, R represents the spot diameter, and P (t) represents the relationship between pressure and time, as shown in Figure 16.

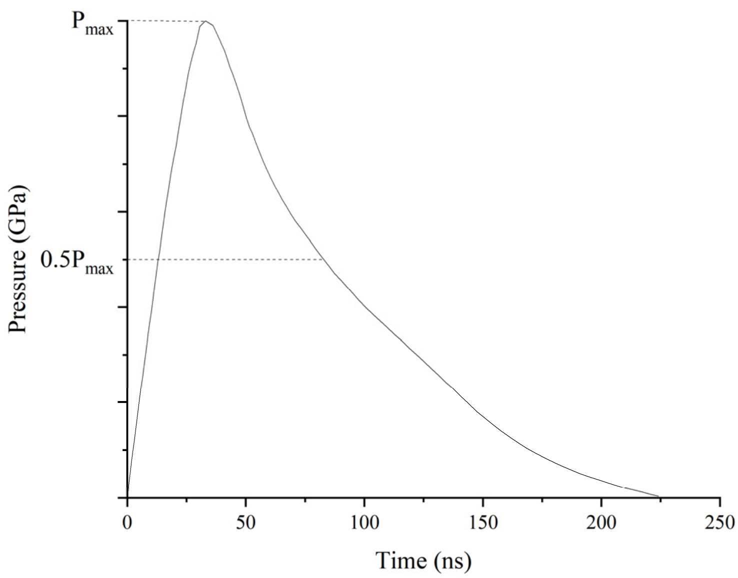

Figure 16. The relationship between pressure and time [43].

When the laser spot is circular, $\mathbf{r}'$ denotes the radius of the circular spot. However, when the laser beam is obliquely incident, the circular laser spot becomes elliptical with an incident angle of θ, a short axis radius of $\mathbf{r}'$, and a long axis radius of R = $\frac{\mathbf{r}'}{\cos\theta}$. As the incident angle increases, the laser-induced shock wave decreases and dissipates horizontally. Consequently, the resulting residual stress and hardness enhancement are reduced [44].

According to Figures 11–13, the untreated sample primarily undergoes abrasive and oxidative wear during the wear process, and its microscopic characteristics include micro-cutting/micro-furrowing marks and oxides on the wear surface. This is primarily because, during the wear process, the temperature generated by low-speed sliding can reach 20–800 °C, causing the material surface to rapidly oxidize. The oxidized material is then removed by the friction balls in the subsequent wear process, with some fragments falling off and becoming abrasive particles. During the reciprocating friction process, the abrasive particles can leave micro-cutting/micro-furrowing marks on the material surface. These particles are eventually crushed and spread over the surface, forming irregular attachments with a high oxygen content. Continuous scratching exposes new surfaces of the matrix, which keeps the oxygen content low.

After plasma nitriding and LSP, the wear patterns of the sample remain largely unchanged, exhibiting abrasive and oxidative wear. However, the wear scar width becomes narrower and the depth shallower due to increased sample surface hardness and effective residual compressive stress. Previous research has shown that the wear resistance of metal materials under abrasive wear is always proportional to their microhardness [45,46]. The LSP process can cause plastic deformation, increased dislocations, and refined grains on material surfaces. According to the classical Hall-Petch theory, the smaller the size of ferrite grains, the higher the yield strength of materials. This is because the smaller the grain size, the more limited the free path of dislocation motion and the greater the difficulty of plastic deformation spreading to adjacent grains [47]. Additionally, generating effective residual compressive stress on material surfaces and sub-surfaces can counteract the local tensile stress generated by reciprocating friction and wear, slow down the propagation of cracks during friction and wear, and transform them into non-propagating cracks. Therefore, during friction and wear, sample surfaces are less likely to suffer extensive damage, leading to improved wear resistance [48]. Higher hardness, refined grains, and higher residual compressive stress enhance the wear resistance of materials.

To intuitively reflect the advancement of the plasma nitriding combined with inclined LSP (NLSP1) composite process proposed in this paper, the experimental methods and quantitative performance indicators of typical laser shock and plasma nitriding modification technologies reported in the recent literature are summarized in Table 4.

Chen et al. [49] adopted single vertical LSP on 20CrNiMo steel, only gaining 25%–30% hardness improvement via plastic deformation. Vertical incidence easily produces residual stress holes, leading to uneven strengthening on inner curved surfaces without nitride hard phases.

Cao et al. [50] combined LSP and nitrogen ion implantation on M50 steel to raise hardness by 68.04%. However, the ion-modified layer is merely ~130 nm thick with uneven nitrogen distribution, restricting long-term wear resistance.

Liu et al. [51] carried out triple vertical LSP on brass with a 38.10% hardness increment. Lacking hard nitrides, the alloy shows severe wear under sliding conditions and cannot process complex inner structures.

Li [44] optimized a single 30° oblique LSP for the FGH95 superalloy, achieving only 24.56% hardness and 17.47% residual stress growth. The absence of a nitrided diffusion layer limits its tribological performance.

Chu et al. [52] applied two-pass LSP before plasma nitriding on TC4 alloy and improved hardness by 23.6%. The pre-shock mode cannot strengthen finished nitride layers, and vertical LSP fails to homogenize inner cavity surfaces.

Different from all the above single or pre-treatment methods, this work performs inclined laser shock after plasma nitriding. The composite sample NLSP1 reaches a 145.2% hardness rise, uniform deep compressive stress and greatly reduced wear depth, realizing synergistic strengthening for complex mold inner surfaces.

Table 4. Comparative summary of relevant LSP and nitriding strengthening studies.

Authors	Experimental Method	Quantitative Experimental Results
Chen et al. [49]	Single vertical laser shock peening (LSP)	Only plastic deformation hardening, hardness increased by about 25%–30%.
Cao et al. [50]	LSP + nitrogen ion implantation composite strengthening	1. Nano-hardness increased from 7.51 GPa to 12.62 GPa (+68.04%); 2. Maximum surface compressive residual stress: −1276.13 MPa.
Liu et al. [51]	Three times single vertical LSP under 6.5 J laser energy	1. Microhardness rises from 107 HV to 145 HV (+38.10%); 2. Wear depth reaches 8.6 μm at 10 mm/s sliding speed.
Li et al. [44]	Oblique laser shock peening (30° incident angle)	1. Surface microhardness increased by 24.56% compared with substrate; 2. Surface compressive residual stress improved by 17.47%.
Chu et al. [52]	Two passes of LSP pretreatment + plasma nitriding (2LSP + PN)	1. Surface microhardness improved by 23.6% compared with Sub + PN; 2. wear rate cut down by 65.1%.

5. Conclusions

This study systematically investigated the synergistic effects of plasma nitriding and OLSP on the microstructural evolution, mechanical properties, residual stress state, and tribological behavior of H13 steel. The main conclusions are summarized as follows:

(1) Plasma nitriding provided an effective strengthening foundation for subsequent OLSP treatment by forming a hardened diffusion layer (~70 μm) without the formation of a brittle compound layer. The increased surface hardness improved the resistance of H13 steel against plastic deformation during sliding contact, providing a favorable substrate for further laser-induced strengthening.

(2) OLSP induced severe plastic deformation in the nitrided surface layer, resulting in grain refinement, increased dislocation accumulation, and enhanced surface mechanical properties. The synergistic strengthening effects associated with grain boundary strengthening and dislocation strengthening contributed to the improvement of surface hardness and deformation resistance.

(3) OLSP significantly modified the residual stress state of plasma-nitrided H13 steel by introducing high-magnitude compressive residual stress. The maximum compressive residual stress reached approximately −1033 MPa after NLSP1 treatment. However, increasing the laser incidence angle reduced the strengthening efficiency due to decreased laser energy coupling and shock pressure transfer, leading to a gradual relaxation of the induced compressive stress.

(4) The combined plasma nitriding and OLSP treatment significantly enhanced the tribological performance of H13 steel. Among all investigated conditions, the NLSP1 specimen exhibited the superior wear resistance, characterized by the minimum wear track width, wear depth, wear volume, and specific wear rate. This improvement was mainly attributed to the synergistic effects of enhanced hardness, grain refinement, dislocation strengthening, and compressive residual stress. These strengthening mechanisms collectively improved the resistance to plastic deformation and suppressed crack initiation, material delamination, and material removal during the sliding wear process.

https://doi.org/10.3390/coatings16070874

The results demonstrate that the effectiveness of OLSP is strongly dependent on the laser incidence angle. An optimized incidence angle promotes efficient laser energy coupling and facilitates the simultaneous generation of grain refinement and compressive residual stress strengthening. OLSP demonstrates immense potential for practical applications in treating complex mold geometries, particularly for critical regions such as deep cavities, fillets, and undercuts that are inaccessible to conventional orthogonal peening.

Author Contributions: L.L.: conceptualization, methodology, investigation, data curation, formal analysis, writing—original draft, writing—review and editing. D.L.: writing—original draft, writing—review and editing, funding acquisition, methodology. J.L.: supervision. J.C.: visualization. Z.X.: methodology, supervision. S.C.: formal analysis. Q.J.: methodology. X.C.: methodology, funding acquisition. W.J.: investigation. W.M.: validation. All authors have read and agreed to the published version of the manuscript.

Funding: Key Research and Development Program of Fujian Province for Ocean and Fisheries (Grant No. FJHYZ-2026-01-004), Synergetic Innovation Special Program of Fuxiaquan National Independent Innovation Demonstration Zone (Grant No.3502ZCQXT2023009).

Data Availability Statement: Data are contained within this article.

Conflicts of Interest: The authors declare no conflicts of interest.

References

1. Deng, J.; Wang, G.; Qi, H.; Ma, H.; Huang, Z. Excellent isotropic mechanical properties of electron beam melted H13 tool steel: Process optimization and microstructural control. *J. Mater. Process. Technol.* **2025**, *336*, 118980. [CrossRef]
2. Birol, Y. Sliding Wear of CrN, AlCrN and AlTiN Coated AISI H13 Hot Work Tool Steels in Aluminium Extrusion. *Tribol. Int.* **2013**, *57*, 101–106. [CrossRef]
3. Birol, Y. Analysis of Wear of a Gas Plasma-nitrided H13 Tool Steel Die in Aluminium Extrusion. *Eng. Fail. Anal.* **2012**, *26*, 203–210. [CrossRef]
4. Terčelj, M.; Smolej, A.; Fajfar, P.; Turk, R. Laboratory Assessment of Wear on Plasma-Nitrided Surfaces of Dies for Hot Extrusion of Aluminium. *Tribol. Int.* **2007**, *40*, 374–384. [CrossRef]
5. Gecu, R. Combined Effects of Cryogenic Treatment and Tempering on Microstructural and Tribological Features of AISI H13 Steel. *Mater. Chem. Phys.* **2022**, *292*, 126802. [CrossRef]
6. Divagar, S.; Sudhahar, M.; Kannan, T.T.M.; Vijayakumar, P.; Tamizhselvan, R. Enhancement of Wear Resistance in Aisi H13 Tool Steel by Liquid Carburizing. *J. Emerg. Technol.* **2020**, *7*, 156–160.
7. Fernandes, F.A.P.; Heck, S.C.; Picone, C.A.; Casteletti, L.C. On the Wear and Corrosion of Plasma Plasma-nitrided AISI H13. *Surf. Coat. Technol.* **2020**, *381*, 125216. [CrossRef]
8. Zhuang, K.; Wan, L.; Weng, J.; Wu, Z.; Zhang, Y.; Tian, C.; Yang, Y. A new elastic abrasive jet machining method for post–treatment of tool coatings: A case study on TiAlN coated tools for titanium machining. *Tribol. Int.* **2023**, *185*, 108533. [CrossRef]
9. Beake, B.D. The influence of the H/E ratio on wear resistance of coating systems—Insights from small-scale testing. *Surf. Coat. Technol.* **2022**, *442*, 128272. [CrossRef]
10. Li, N.; Wang, Q.; Niu, W.; Han, P.; Guo, N.; Li, S. Microstructure and wear behaviors of 17-4 PH stainless steel fabricated by laser cladding with post LSP treatment. *Wear* **2024**, *538*, 205207. [CrossRef]
11. Miao, H.; Mei, Q.; Yuan, J.; Zheng, Z.; Jin, Y.; Zuo, D. Low Cycle Fatigue and Strengthening Mechanism of Cold Extruded Large Diameter Internal Thread of Q460 Steel. *Chin. J. Mech. Eng.* **2016**, *29*, 556–563. [CrossRef]
12. Dang, J.; Zhang, H.; An, Q.; Lian, G.; Li, Y.; Wang, H.; Chen, M. Surface Integrity and Wear Behavior of 300M Steel Subjected to Ultrasonic Surface Rolling Process. *Surf. Coat. Technol.* **2021**, *421*, 127380. [CrossRef]
13. Zhang, Z.; Yang, Y.; Gao, Y.; Wang, G.; Shi, W. Performance Analysis of 7075 Aluminum Alloy Strengthened by Cavitation Water Jet Peening at Different Scanning Speeds. *Crystals* **2022**, *12*, 1451. [CrossRef]
14. Liang, H.; Pan, Y.Z.; Sun, Y.H.; Zhang, Y.J.; Pan, Y.; Fu, X.L. Review of research on ultrasonic rolling surface composite strengthening. *Surf. Technol.* **2024**, *53*, 41–55+109.
15. Zhu, Y.R. Application of cold extrusion of slotted bushing in superhigh strength steel and high strength aluminum alloy lamination. *Sci. Technol. Horiz.* **2020**, 104–106. [CrossRef]
16. Lin, Z.; Bai, Q.S.; Wang, H.F.; Tang, W.; Wu, B. Research progress on strengthening mechanism and fatigue life of cold extrusion of hole bushing. *Surf. Technol.* **2023**, *52*, 1–14+99. [CrossRef]

17. Qian, X.; Jiang, Y.Y.; Guan, S.M.; Li, Z.F. Review of tightening hole strengthening technology for aircraft structural parts. *Mech. Strength* **2011**, *33*, 749–753. [CrossRef]
18. Ma, Y.; Zhai, L.B.; Zhu, Z.H.; Zhang, Y.B.; Liu, L.R.; Ma, S.G. Research progress of surface modification technology of water jet. *Aeronaut. Manuf. Technol.* **2021**, *64*, 28–35. [CrossRef]
19. Zhou, W.; Ren, X.; Yang, Y.; Tong, Z.; Chen, L. Tensile Behavior of Nickel with Gradient Microstructure Produced by LSP. *Mater. Sci. Eng. A* **2020**, *771*, 138603. [CrossRef]
20. Wang, F.; Ding, Z.; Li, H.; Ding, C.; Zhang, D.; Shan, D.; Guo, B.; Xu, J. Impact of laser shock peening on the microstructure and mechanical performance of 7075 aluminum alloy. *J. Mater. Res. Technol.* **2025**, *37*, 1472–1485. [CrossRef]
21. Yin, M.; Cai, Z.; Li, Z.; Zhou, Z.; Wang, W.; He, W. Improving Impact Wear Resistance of Ti-6Al-4V Alloy Treated by LSP. *Trans. Nonferrous Met. Soc. China* **2019**, *29*, 1439–1448. [CrossRef]
22. Dai, F.Z.; Lu, J.Z.; Zhang, Y.K.; Wen, D.P.; Ren, X.D.; Zhou, J.Z. Effect of laser spot size on the residual stress field of pure Al treated by laser shock processing: Simulations. *Appl. Surf. Sci.* **2014**, *316*, 477–483. [CrossRef]
23. Peyre, P.; Fabbro, R.; Merrien, P.; Lieurade, H.P. Laser shock processing of aluminium alloys. Application to high cycle fatigue behaviour. *Mater. Sci. Eng. A* **1996**, *210*, 102–113. [CrossRef]
24. Lin, C.H.; Wu, H.B.; Li, Z.G.; Yu, L.W.; Zeng, J.L.; Xia, C.P.; Liao, Y.F.; Xu, H.S.; Zhang, Y.K. Evaluation of oblique LSP effect of FGH95 superalloy turbine disk material. *Mater. Today Commun.* **2022**, *31*, 103534. [CrossRef]
25. Wu, J.; Zhou, Z.; Lin, X.; Qiao, H.; Zhao, J.; Ding, W. Improving the wear and corrosion resistance of aeronautical component material by laser shock processing: A review. *Materials* **2023**, *16*, 4124. [CrossRef] [PubMed]
26. Fabbro, R.; Fournier, J.; Ballard, P.; Devaux, D.; Virmont, J. Physical study of laser-produced plasma in confined geometry. *J. Appl. Phys.* **1990**, *68*, 775–784. [CrossRef]
27. Gur, H.C.; Pan, J. *Handbook of Thermal Process Modeling Steels*; Taylor and Francis: Abingdon-on-Thames, UK; CRC Press: Boca Raton, FL, USA, 2008.
28. Duan, X.; Yu, L.; Ding, G.; Cai, S.; Dai, L.; Jiang, M. Shock wave response of amorphous solids by mesoscale simulations. *Sci. Sin. Phys. Mech. Astron.* **2025**, *55*, 286122. [CrossRef]
29. Wang, J.; Xu, Z.; Lu, X. Effect of the Quenching and Tempering Temperatures on the Microstructure and Mechanical Properties of H13 Steel. *J. Mater. Eng. Perform.* **2020**, *29*, 1849–1859. [CrossRef]
30. Mansilla, C.; Ocelík, V.; De Hosson, J. Local residual stress measurements on nitride layers. *Mater. Sci. Eng. A* **2015**, *636*, 476–483. [CrossRef]
31. Nie, X.; He, W.; Zang, S.; Wang, X.; Zhao, J. Effect study and application to improve high cycle fatigue resistance of TC11 titanium alloy by LSP with multiple impacts. *Surf. Coat. Technol.* **2014**, *253*, 68–75. [CrossRef]
32. Berg, M.; Budtz-Jørgensen, C.V.; Reitz, H.; Schweitz, K.O.; Chevallier, J.; Kringhøj, P.; Bøttiger, J. On Plasma Nitriding of Steels. *Surf. Coat. Technol.* **2000**, *124*, 25–31. [CrossRef]
33. Zhang, Y.K.; Zuo, D.W.; Zhang, L.; Kong, D.J.; Zhou, J.Z.; Feng, A.X.; Zhang, L.F.; Ge, T.; Ren, X.D. Study on Deformation Behaviors of LD31 (6063) Aluminum Alloy Sheet by Oblique Angle Laser Shock. *Key Eng. Mater.* **2006**, *315–316*, 511–515. [CrossRef]
34. Hou, L.; Wei, Y.; Shu, X.; Xu, B. Nanocrystalline Structure of Magnesium Alloys Subjected to High Energy Shot Peening. *J. Alloys Compd.* **2010**, *492*, 347–350. [CrossRef]
35. Broszeit, E.; Matthes, B.; Herr, W.; Kloos, K. Tribological properties of r.f. sputtered Ti-B-N coatings under various pin-on-disc wear test conditions. *Surf. Coat. Technol.* **1993**, *58*, 29–35. [CrossRef]
36. Cao, Z.; Cui, L.; Luo, S.; Su, H.; Pang, Z.; Zhao, W.; Zhang, L.; He, W.; Liang, X. Superior fretting wear resistance of titanium alloys from stable gradient nanostructures induced by LSP. *Int. J. Plast.* **2025**, *188*, 104293. [CrossRef]
37. Li, H.; Hsu, E.; Szpunar, J.; Utsunomiya, H.; Sakai, T. Deformation Mechanism and Texture and Microstructure Evolution during High-Speed Rolling of AZ31B Mg Sheets. *J. Mater. Sci.* **2008**, *43*, 7148–7156. [CrossRef]
38. He, T.; Liu, Z.; Li, L.; Xiong, Y.; Du, S.; Zhang, Y. Effect of Supersonic Fine Particle Bombardment on Microstructure Evolution and Tribological Properties of GCr15SiMn Bearing Steel. *J. Mater. Res. Technol.* **2024**, *28*, 1111–1120. [CrossRef]
39. Leite, M.V.; Figueroa, C.A.; Gallo, S.C.; Rovani, A.C.; Basso, R.L.O.; Mei, P.R.; Baumvol, I.J.R.; Sinatora, A. Wear Mechanisms and Microstructure of Pulsed Plasma Plasma-Nitrided AISI H13 Tool Steel. *Wear* **2010**, *269*, 466–472. [CrossRef]
40. Binder, C.; Bendo, T.; Hammes, G.; Klein, A.N.; De Mello, J.D.B. Effect of Nature of Nitride Phases on Sliding Wear of Plasma Plasma-Nitrided Sintered Iron. *Wear* **2015**, *332–333*, 995–1005. [CrossRef]
41. Jacobsen, S.D.; Hinrichs, R.; Baumvol, I.J.R.; Castellano, G.; Vasconcellos, M.A.Z. Depth Distribution of Martensite in Plasma Plasma-nitrided AISI H13 Steel and Its Correlation to Hardness. *Surf. Coat. Technol.* **2015**, *270*, 266–271. [CrossRef]
42. Wang, B.; Zhao, X.; Li, W.; Qin, M.; Gu, J. Effect of Plasma-Nitrided-Layer Microstructure Control on Wear Behavior of AISI H13 Hot Work Die Steel. *Appl. Surf. Sci.* **2018**, *431*, 39–43. [CrossRef]
43. Zagonel, L.F.; Figueroa, C.A.; Droppa, R.; Alvarez, F. Influence of the Process Temperature on the Steel Microstructure and Hardening in Pulsed Plasma Nitriding. *Surf. Coat. Technol.* **2006**, *201*, 452–457. [CrossRef]

44. Tong, Z.; Liu, H.; Jiao, J.; Zhou, W.; Yang, Y.; Ren, X. Microstructure, Microhardness and Residual Stress of Laser Additive Manufactured CoCrFeMnNi High-Entropy Alloy Subjected to LSP. *J. Mater. Process. Technol.* **2020**, *285*, 116806. [CrossRef]
45. Jiang, Y.F.; Wang, F.; Zhu, Y.Y.; Gu, Y.Y.; Lai, Y.L. Study on Forming Characteristics of Metal Sheet by Laser Shock in Oblique Angle. *Key Eng. Mater.* **2010**, *431–432*, 429–433. [CrossRef]
46. Thorslund, T.; Kahlen, F.-J.; Kar, A. Temperatures, Pressures and Stresses during Laser Shock Processing. *Opt. Lasers Eng.* **2003**, *39*, 51–71. [CrossRef]
47. Liu, Y.; Jin, B.; Li, D.-J.; Zeng, X.-Q.; Lu, J. Wear Behavior of Nanocrystalline Structured Magnesium Alloy Induced by Surface Mechanical Attrition Treatment. *Surf. Coat. Technol.* **2015**, *261*, 219–226. [CrossRef]
48. Hu, Y.; Watson, M.; Maiorino, M.; Zhou, L.; Wang, W.J.; Ding, H.H.; Lewis, R.; Meli, E.; Rindi, A.; Liu, Q.Y.; et al. Experimental Study on Wear Properties of Wheel and Rail Materials with Different Hardness Values. *Wear* **2021**, *477*, 203831. [CrossRef]
49. Chen, X.Y.; Li, K.L.; Lin, Y.R.; Xu, Z.; Guo, B.; Chen, J.; Jiang, Q.; Zhao, Z. Effect of laser shock peening uniformity on bending fatigue life of 20CrNiMo. *Opt. Laser Technol.* **2024**, *175*, 110704. [CrossRef]
50. Cao, Z.Y.; He, W.F.; Luo, S.H.; Song, J.; Su, H.; Pang, Z.; Zhao, S.; Liang, X. Effect of combined laser shock peening and nitrogen implantation on the microstructure and tribological properties of M50 bearing steel. *J. Mater. Res. Technol.* **2024**, *30*, 5080–5095. [CrossRef]
51. Liu, L.; Wang, J.J.; Zhou, J.Z. Characterization and analysis on micro-hardness and microstructure evolution of brass subjected to laser shock peening. *Opt. Laser Technol.* **2019**, *115*, 325–330. [CrossRef]
52. Li, C.; Luo, J.; Zhao, Z.; Xu, J. Effect of laser shock peening pretreatment on the microstructure and wear resistance of plasma nitrided TC4 titanium alloy. *Surf. Coat. Technol.* **2025**, *512*, 132337. [CrossRef]